Contents lists available at ScienceDirect

Engineering Geology

journal homepage: www.elsevier.com/locate/enggeo

Internal structure and deformation of an unstable crystalline rock mass above Randa (Switzerland): Part I — Internal structure from integrated geological and geophysical investigations

Heike Willenberg [a], Simon Loew [a,*], Erik Eberhardt [a,1], Keith F. Evans [a], Thomas Spillmann [b,2], Björn Heincke [b,3], Hansruedi Maurer [b], Alan G. Green [b]

[a] Geological Institute, Swiss Federal Institute of Technology, ETH Hoenggerberg, Zürich, Switzerland
[b] Institute of Geophysics, Swiss Federal Institute of Technology, ETH Hoenggerberg, Zürich, Switzerland

ABSTRACT

In 1991, the steep slope above the village of Randa in southern Switzerland failed during two successive rockslide events three weeks apart. The failures, which resulted in the release of approximately $30 \times 10^6 \, m^3$ of material, occurred in fractured gneissic rock whose principal foliation, faults and fracture zones dip into the slope. Above the scarp of the second rockslide, the mountain continues to move at rates of up to 2 cm/year. In an attempt to understand failure mechanisms in fractured crystalline rock masses, we have carried out a comprehensive multidisciplinary study that included detailed geological mapping, borehole logging and imaging, and surface and borehole geophysical surveys. An integrated interpretation of the resultant data has revealed the presence of three prominent fault- and fracture zone sets that define the internal structure of the rock mass. Some faults and fracture zones could be traced up to 85 m into the subsurface using borehole radar reflection methods. The dips of the faults and fracture zones estimated from surface mapping matched those from radar reflection and borehole televiewer surveys. No evidence was found for significant faults or persistent weakness planes that paralleled the 1991 rockslide failure surfaces. Instead, the new observations were consistent with dominant failure mechanisms that involve the progressive development of major shear and brittle fracture zones and the eventual destruction of intact rock bridges immediately prior to catastrophic collapse. This integrated study provides the first reliable model of the 3-D fault structure associated with and contributing to a large rock slope instability in a brittle crystalline rock mass.

© 2008 Elsevier B.V. All rights reserved.

1. Introduction

Landslide hazard evaluation and mitigation are becoming increasingly important due to progressive urban development in landslide prone-areas (Schuster, 1996; Petley et al., 2005). Considerable advances have been made concerning the risk management of such hazards with the development of improved mitigation techniques and early warning systems, based for example on displacement monitoring (Voight, 1989; Crosta and Agliardi, 2002) and remote sensing techniques (Tarchi et al., 2003; Metternicht et al., 2005). However, progress would be greatly assisted by more knowledge of the internal structures and mechanisms that control slope movements. This is particularly true for brittle rock masses where deformation rates may suddenly accelerate to catastrophic failure. A challenging class of landslides in this regard concerns those involving rock slopes in which the persistent planes of weakness (bedding, foliation, etc.) dip into the slope. In this situation, the development of a through-going failure surface, which is necessary for coherent slope failure to develop on a significant scale, is obliged to occur through the progressive development of a shear surface stepping up and along non-persistent discontinuities. This is generally a complex process that may involve the fracture of intact rock bridges to link and extend the rupture surface (Einstein et al., 1983). Detailed *in-situ* studies of active slopes are essential to better understand these processes (Hack, 2000; Godio et al., 2006).

In 2001, we established an *in-situ* laboratory on a large slow moving crystalline rock mass located above the village of Randa in the Matter Valley of the Swiss Alps (Fig. 1). One of the key objectives here involved the detailed characterisation of the 3-D geological structure of the rock mass through geological mapping and surface and borehole geophysics. The results of this characterisation are reported in this paper.
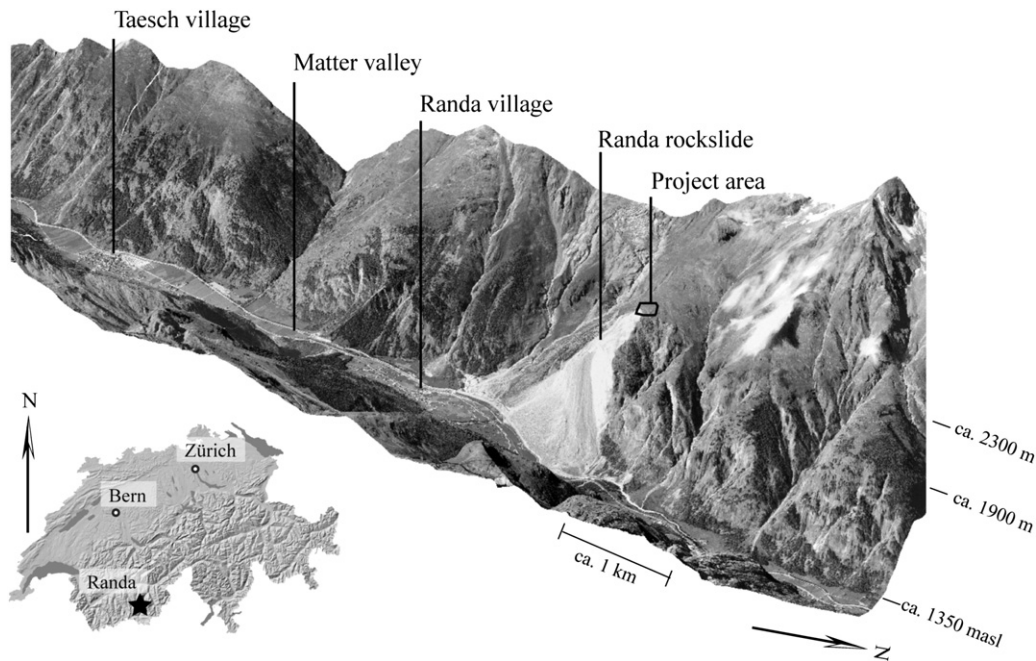
Fig. 1. Digital elevation model (DEM, 1:25,000) showing the location of the Randa project area on the western slope of the Matter valley. The DEM and orthophoto are reproduced with permission of Swisstopo (BA068088).

The moving rock mass is situated immediately above the scarp of a major, multiple-event rockslide that occurred in 1991. It involved a total rock volume of about 30 million m³. Since then, the remaining unstable rock mass has been moving at a rate of up to 2 cm/year (Jaboyedoff et al., 2004; Ornstein et al., 2005). Estimates of the currently mobile rock volume range between 3 and 9 million m³ (Ischi et al., 1991). Our study included the drilling of 3 moderately deep (50–120 m) and 9 shallow (0.5–5 m) research boreholes into the moving rock mass that were then used as part of a comprehensive monitoring and site characterisation program.

In this paper, we describe the internal structure of the active rock mass as determined from geological mapping, borehole fracture imaging, and surface and borehole radar surveys. After presenting relevant background information, we describe briefly each of the geological and geophysical methods applied in the study and then report the results. Finally, the results are integrated to obtain a description of the 3-D internal structure of the unstable rock mass. Displacements occurring on these structures are described in the companion paper (hereafter referred to as Part II).

2. Background

2.1. Geological setting

The Randa study site is located within the gneissic series of the Siviez–Mischabel nappe. The gneisses consist of a metamorphosed Permian porphyritic alkaline to subalkaline granitic intrusion (referred locally to as the Randa augengneiss) that is located within polycyclic Palaeozoic gneisses, schists and amphibolites. On the investigated slope, the main augengneisses outcrop from the valley bottom to their contact with a series of overlying heterogeneous gneisses and schists at approximately 1900 m above sea level (masl) elevation (Fig. 1).

Generally, the structure of the Siviez–Mischabel nappe is referred to as a large recumbent fold (Bearth, 1964; Müller, 1983). In the project area, which belongs to the weakly deformed normal limb of the fold nappe, foliation dips gently to the SW, away from the valley and into the slope. Kinematically, this favours rock slope stability.

2.2. The 1991 rockslide events

The 1991 rockslide occurred as a succession of two large events on April 18th and May 09th, 1991 (Fig. 2), which together involved a total rock volume of about 30 million m³. Both events were themselves multiphase events lasting several hours (Schindler et al., 1993). Some precursory activity was noticed prior to the first event. This included increased rockfall activity during the preceding winter and larger rockfalls and intense water flow from daylighting fractures on the steep rock face some days to weeks earlier (Schindler and Eisenlohr, 1992). Nevertheless, the first rockslide was generally reported as unexpected and no monitoring systems were in place to constrain the rock mass behaviour during the lead-up to failure.

The first event primarily involved the collapse of the massive augengneiss cliff comprising the lower half of the slope (Fig. 2). A large NE-dipping fault close to the valley floor (Fig. 3) has been proposed as the basal shear plane for the first event with subsequent sliding of
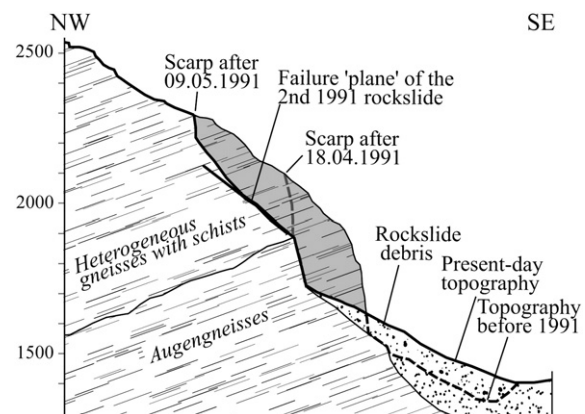

Fig. 2. Cross-section of the 1991 rockslides modified after Wagner (1991) and Eberhardt et al. (2004), the failed rock mass is shown shaded. The failure 'plane' of the 2nd event is covered with debris above 1900 m and thus may not be as linear as shown.
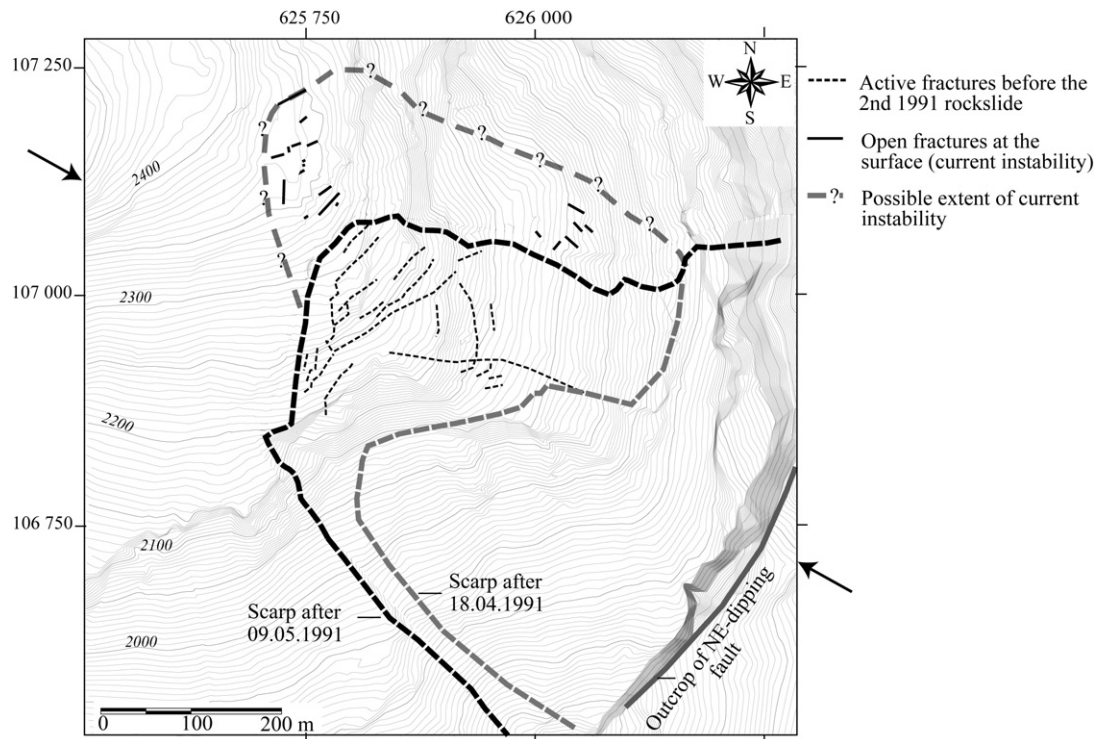
Fig. 3. Topographic map of the project area before the 1991 rockslides. The tops of the scarps of the two main rockslide events (April 18 and May 9, 1991) are indicated. The thin dotted lines are surface fractures that were seen to be active between the first and second rockslide events. The thin solid lines denote open surface fractures on the currently moving rock mass to the north and northwest of the rockslide scarp. The extent of the current instability NW of the 1991 rockslide scarp is based on geodetic monitoring data, which is described in detail in the companion paper (Part II). The NE-dipping fault indicated close to the valley floor is proposed to have acted as a basal sliding surface for the first 1991 rockslide event. The arrows indicate the location of the section shown in Fig. 2.

adjacent blocks in the SE direction along fractures dipping 40–50° to the SE (mean orientation 110°/45°) (Wagner, 1991; Sartori et al., 2003). The second event occurred in the overlying heterogeneous gneisses and formed a large SE-dipping failure surface (Fig. 2). Rudimentary displacement and fracture monitoring systems installed on the unstable rock mass shortly after the first event provided information
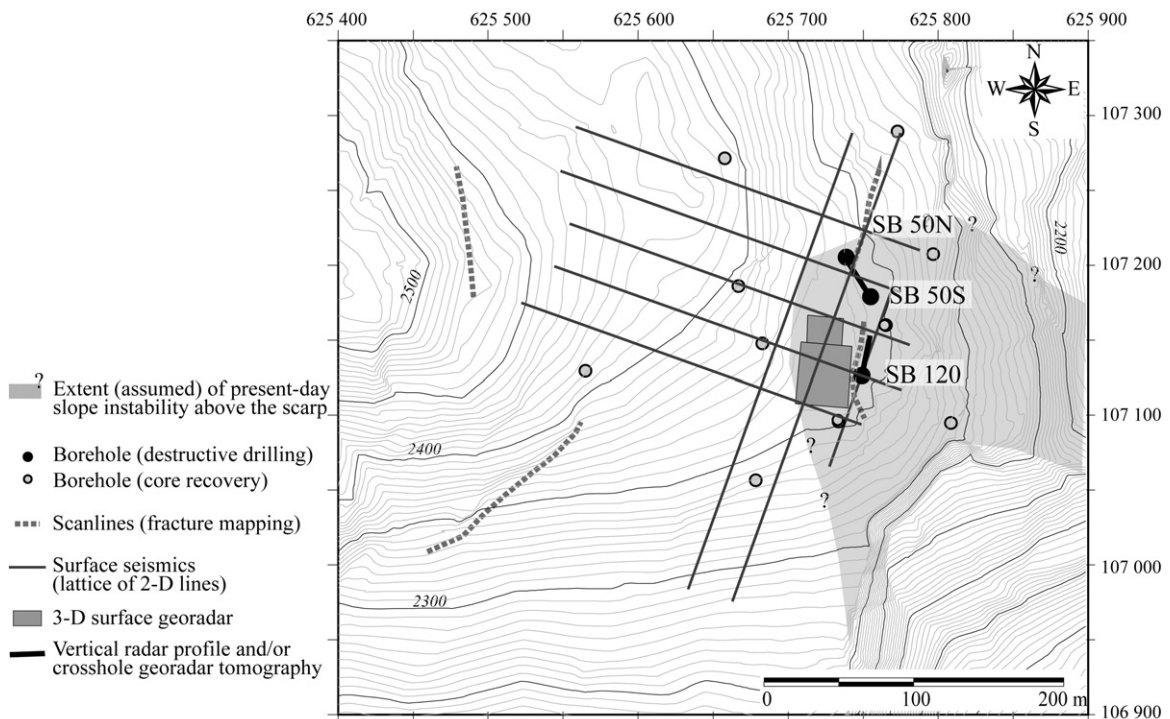

Fig. 4. Location of the geological and geophysical survey areas. The focus of the investigations was the upper part of the unstable rock mass, where the three deep exploratory boreholes (SB 120, SB 50S and SB 50N) were drilled.
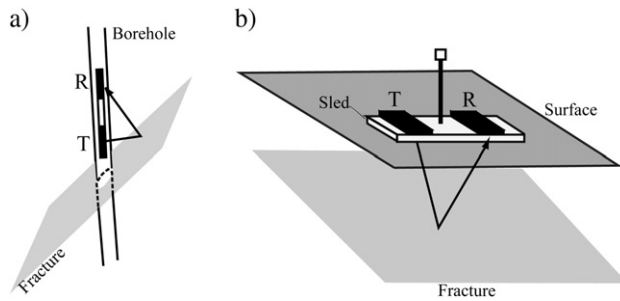
Fig. 5. Illustration of borehole and surface georadar methods employed: a) Single-hole georadar reflection measurement. The radar system, which contains both a transmitter (T) and receiver (R) antenna, is moved along the borehole axis taking measurements every 10 or 20 cm (modified after Spillmann et al., 2007a); b) Surface georadar surveys in which the transmitter and receiver antenna are mounted on a sled together with a prism for determining the 3-D position of the sled at each measurement point using a self-tracking theodolite (modified after Heincke et al., 2005).

about the deformation leading up to the second event. Several fractures oriented NE–SW, N–S or W–E were seen to be opening (Fig. 3) (Schindler et al., 1993). Further details of this 1991 monitoring network are given in Part II.

Sartori et al. (2003) and Jaboyedoff et al. (2004) have suggested that the SE-dipping failure surface corresponded to a persistent, pre-existing failure plane. In contrast, Schindler et al. (1993) deduced from the long duration of the rockslide events that sliding occurred parallel to

non-persistent fractures. Eberhardt et al. (2004) presented a series of modelling studies on the long term destabilisation of the rock mass. They attempted to reproduce the post-failure geometry of the slope, and suggested that progressive failure of the slope through rock mass strength degradation mechanisms contributed to the catastrophic failure.

No external factor that might have served to trigger the 1991 rockslide events has been identified. The climatic record for the meteorological station in the Matter Valley showed no unusual environmental conditions (e.g. intensive precipitation or snow melt) at the time (Eberhardt et al., 2001). Seismographic records allowed earthquake triggering to be ruled out. Similarly, melting of permafrost within the failed rock mass was considered unlikely, since statistical modelling of the permafrost distribution in the upper Matter valley suggested that none was present in the immediate rockslide area (Gruber and Hoelzle, 2001).

Following the 1991 rockslides, the rock mass to the north and northwest of the rockslide scarp has continued to show displacements to the SE at a maximum rate of 2 cm/year. The areal extent of the moving mass shown in Fig. 3 has been constrained with periodically-measured benchmark arrays across surface fractures and geodetic monitoring of a large retro-reflector network (Jaboyedoff et al., 2004; Ornstein et al., 2005).

3. Geological investigation methods

3.1. Geological field mapping

Field mapping has focussed on the area surrounding the 1991 rockslide scarp. Due to the limited accessibility, areas north of the
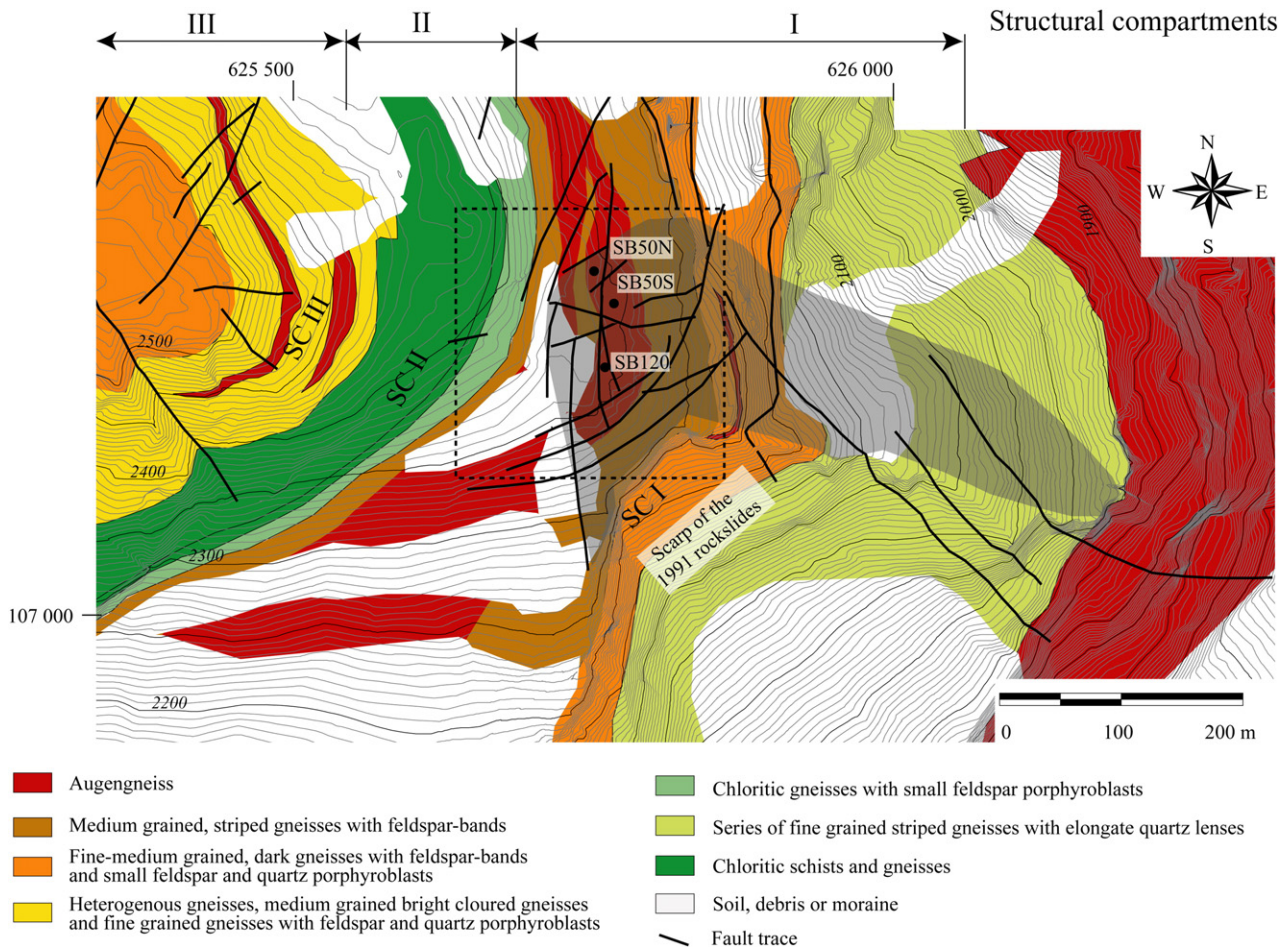

Fig. 6. Traces of surface faults and fracture zones superimposed on a lithological map. The structural compartments indicated at the top of the map correspond to areas with similar small-scale fracture orientations. They generally follow the lithological boundaries. The assumed extent of the unstable rock mass is shown shaded. The dashed box denotes the extent of Fig. 10. The digital elevation model was provided by CREALP.

a) SC I N = 839   N = 310

b) SC II N = 309   N = 48
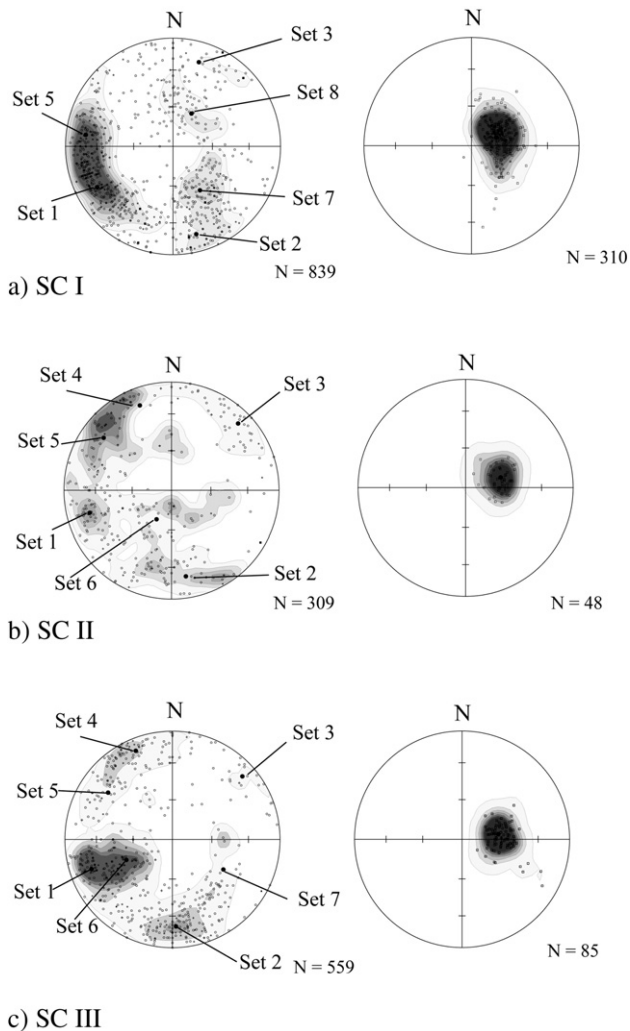

c) SC III N = 559   N = 85

Fig. 7. Orientation distributions of fractures (left) and foliation fractures (right) in each of the three structural compartments: a) For SC I, which includes the unstable rock mass. Fracture sets 4 and 6 are absent from SC I, whereas fractures from set 8 are more frequent. b) For SC II, which corresponds to the chloritic gneisses and schists, fracture sets 7 and 8 are absent. c) For SC III, which is situated above the unstable rock mass and the chloritic gneisses and schists, fracture sets 1–7 are present. The projections are lower hemisphere.

scanline mapping followed procedures recommended by Priest (1993). In this paper, only the orientation data is presented; for analyses of the normal set spacing and mean trace length see Willenberg (2004).

The subsurface investigations included a 120-m and two 50-m deep, pneumatically drilled boreholes (denoted as SB 120, SB 50S and SB 50N in Fig. 4). The locations of the three boreholes were chosen based on existing monitoring results, drilling logistics, the spatial requirements for active crosshole seismic and radar experiments and surface topography. The holes were found to be dry except for the lowermost 10 m of SB 120. After drilling, a suite of wireline logs was run. They consisted of a 4-arm borehole geometry log for determining the hole trajectory (azimuth and inclination) and cross-section, a spectral gamma log for identification of lithology, and an optical televiewer (OTV) log to provide oriented images of the borehole wall. Minor and major fractures were distinguished on the basis of the thickness of their traces in the OTV images. Schistose bands or fractures with openings >2 mm were regarded as major fractures and hence classified as faults. Full-waveform sonic logs were also run in the 50 m boreholes after PVC inclinometer casing had been cemented in place and could be filled with water.

The mechanical properties of the various lithologies were obtained by testing the core samples recovered from the nine 0.5–5 m deep boreholes drilled for the installation of shallow seismic sensors (locations shown in Fig. 4). Static Young's modulus and Poisson's ratio were determined from uniaxial and triaxial compression tests performed at the University of Saskatchewan's (Canada) Rock Mechanics Laboratory. P- and S-wave velocities were measured in-house under different hydrostatic pressures (Heincke et al., 2006b).

4. Geophysical investigation methods

4.1. Borehole georadar experiments

Borehole georadar data were recorded in each of the three deep boreholes using both single-hole radar reflection and vertical radar

scarp below 2300 masl elevation could only be partly mapped. Lithological units were distinguished on the basis of field estimates of quartz–feldspar content, grain size, mica content, petrographic heterogeneity on the decimeter- to meter-scale, and the presence of small-scale deformation structures such as micro-folds. The locations of surface fault and fracture-zone traces were determined from outcrop mapping and the identification of morphologic lineaments. A tectonic structure was mapped as a *fault* if indications of significant differential displacement by brittle failure were found (Ramsay and Huber, 1987), such as the presence of slickensides, Riedel fractures or cataclastic and gouge-type fabrics. Phyllonites (i.e. mm–cm thick densely foliated schistous gneisses) were mapped as *ductile shear zones*. Intense brittle fracturing over dm-wide zones with only minor differential displacement was used to identify *fracture zones*. In terms of their scale, faults and fracture zones could also be distinguished from fractures by their several tens of meters extent.

Outcrop mapping of the small-scale fracture network (i.e. fractures <10 m in length) was performed over the entire mapping area. In addition, scanline measurements were made along four lines of 40–140 m length on large rock faces in various lithologies, both in the unstable and stable parts of the investigated rock mass (see Fig. 4). The
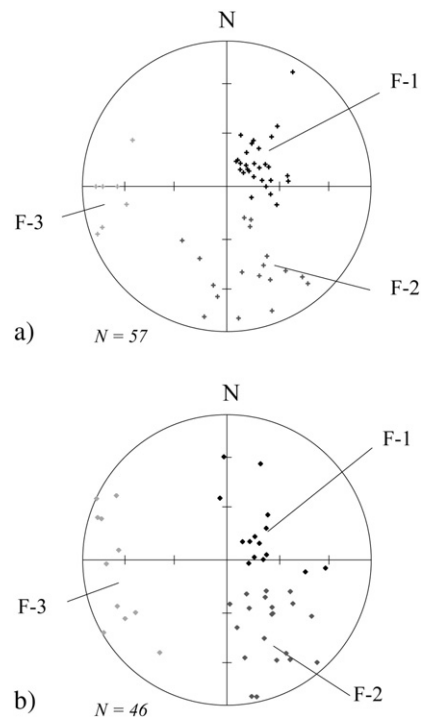

a) N = 57

b) N = 46

Fig. 8. Stereonets showing the poles to faults and fracture zones mapped: a) on surface, and b) in the boreholes. Pure phyllonites parallel to foliation (i.e. without fracture) in the boreholes are not plotted. The projections are lower hemisphere.

profiling (VRP) methods and crosshole techniques. These borehole methods allowed the electromagnetic reflection characteristics of the rock mass to be investigated at depths greater than could be reached using surface georadar approaches. Borehole reflection methods are particularly useful for imaging steeply dipping fractures as shown in Fig. 5a (Olsson et al., 1992; Tronicke and Knoll, 2005). At Randa, it involved the progressive movement of a fixed-offset transmitter–receiver antenna pair (MALA system with 100 MHz antennas) along the borehole. The interpretation of the reflections that intersected the borehole walls was constrained by the televiewer images (Spillmann et al., 2007). Fortunately, some reflections that did not cut the boreholes and hence could not be directly oriented (single-hole georadar images by themselves contain no azimuthal information as to the direction of the reflector) could be projected to faults and fracture zones mapped on surface, thus allowing their orientation to be derived.

The VRP data were gathered in SB 50S and SB 50N along a surface profile between the boreholes, and in SB 120 to a depth of 50.5 m using a surface line that extended out to 28.5 m from the hole towards the north (see Fig. 4). Georadar crosshole tomography between the two 50 m deep boreholes yielded estimates of radar velocity and attenuation between the boreholes (Spillmann et al., 2007). The results of the VRP and crosshole experiments are not reported in this paper as they provided only limited useful data (Spillmann et al., 2007).

4.2. 3-D surface georadar

The 3-D surface georadar technique has the potential to image faults and fracture zones within crystalline rock masses with high resolution and accuracy (Grasmück, 1996), but the penetration depth is usually limited to several tens of meters due to attenuation and
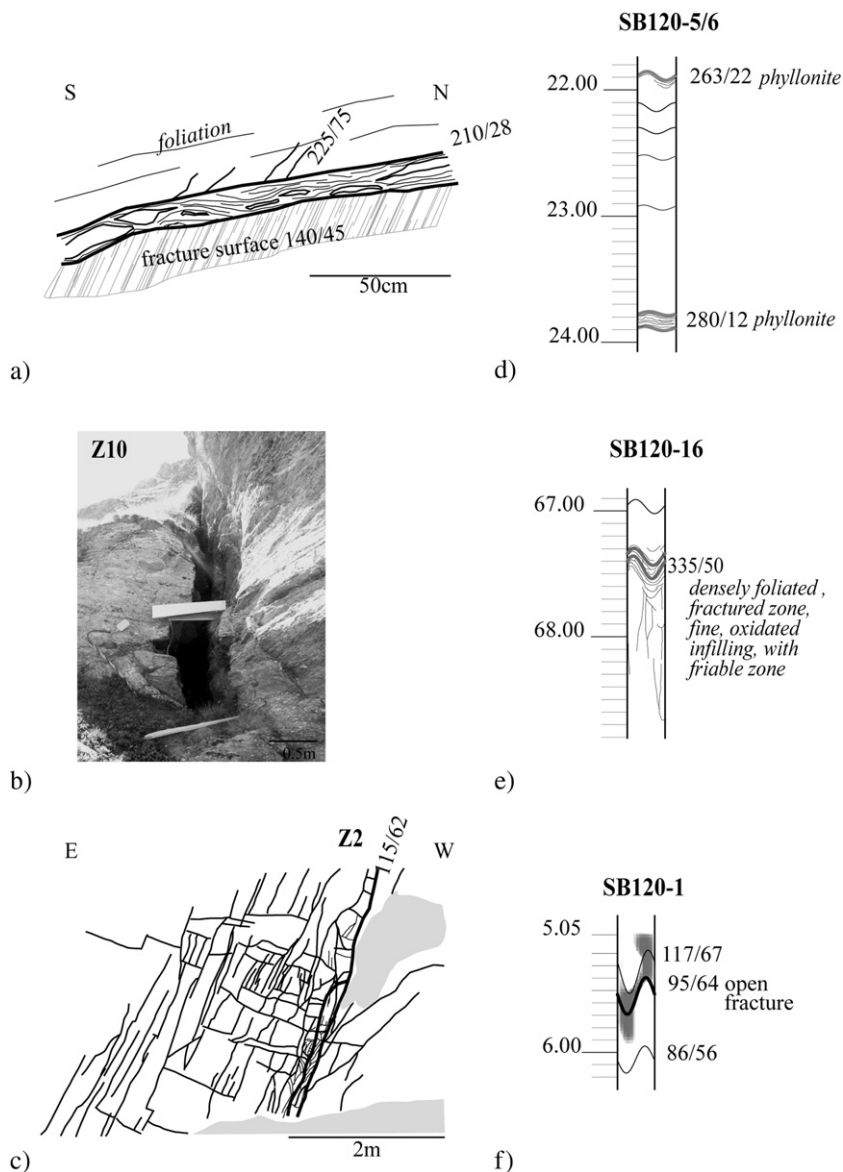

Fig. 9. Outcrop and borehole examples of faults and fracture zones. a) Brittle–ductile shear zone parallel to foliation (set F-1), accompanied by Riedel fractures (top) and set 8 secondary fractures (hatched area below). b) Open surface fracture belonging to an F-2 set fault that is spanned by a crackmeter. c) Brittle–ductile fault of the F-3 set. The central fault core, highlighted by a thick solid line, is accompanied by a fracture zone. d) Sketch of two F-1 faults seen in the borehole OTV logs. Unwrapping of the borehole wall image shows phyllonites oriented parallel to foliation. e) F-2 borehole fault characterised by a 10 cm thick zone of densely foliated and fractured rock. f) Open borehole fracture belonging to an F-3 fracture zone.

scattering effects. The Randa surface georadar data were acquired across two overlapping 480–850 m² areas (Fig. 4). Two unshielded 100 MHz antennae mounted on a sled (Fig. 5b) were used to record data along densely spaced parallel lines (Heincke et al., 2005). After pre-processing, migration of the data accounting for topography produced images of moderately to shallowly dipping features (Heincke et al., 2005). To map steeply dipping structures characterised by rough surfaces, a new scheme that highlighted the presence of diffractions was developed and applied to the georadar data (Heincke et al., 2006a). This new semblance-based migration scheme, which also accounts for the influence of topography, was effective in mapping the locations of numerous steeply dipping structures throughout the depth range of interest.

4.3. 3-D seismic refraction tomography

Unlike the georadar techniques, the 3-D tomographic seismic refraction method does not have the resolution to determine the locations and orientations of discrete fault and fracture zones. However, the distribution of low and high P-wave velocities within the rock mass is a measure of the degree of fracturing. Several case studies using 2-D refraction tomography on unstable rock slopes have previously been reported (Hack, 2000; Godio et al., 2006). To our knowledge, our survey was the first to involve a true 3-D approach (Heincke et al., 2006b).

The Randa seismic survey was designed to cover accessible parts of the unstable rock mass and large regions of the presumed stable mountain slope (Fig. 4). The primary layout involved eight profiles, five oriented in an E–W direction and 3 oriented in a N–S direction. Source and receiver spacings along the 126–324 m long profiles were

4 and 2 m, respectively. By using seven 24-channel 24-bit Geode recording systems, we were able to deploy receivers along the entire length of each profile (i.e. 64–163 receivers depending on the length of profile). To minimise disturbance to the surrounding alpine environment, small shot charges of 5–50 g were detonated in shallow (0.5–0.7 m deep) holes. In addition to the shotholes along the profiles, we also drilled clusters of 8 holes (1 per profile) at 33 locations offset from the profiles. Signals generated by shots detonated at these clusters were recorded on receivers along all profiles (Heincke et al., 2006b). Furthermore, all inline and offset shots were recorded by 3-component geophones deployed in the three moderately deep boreholes and in the nine shallow boreholes from which core samples were obtained (locations shown in Fig. 4). Together, the profiles and offset shots and receivers yielded moderately good to very good coverage of the entire investigation volume (Heincke et al., 2006b).

The P-wave first arrival times were inverted using a 3-D tomography algorithm. Comparison of estimated seismic velocities with those measured on intact core samples allowed Heincke et al. (2006b) to estimate the Seismic Rock Quality Designation (SQRD) (Hack, 2000) of the rock mass.

5. Results

5.1. Lithology and structural compartments

Based on the mapping criteria, seven lithological rock types were distinguished in the study area (Fig. 6). The lithological boundaries were found to follow the foliation, which dips 20–30° to the WSW, as noted by previous studies (Bearth, 1964; Müller, 1983). Lab testing of the *augengneisses* and *striped gneisses with feldspar-bands* both yielded
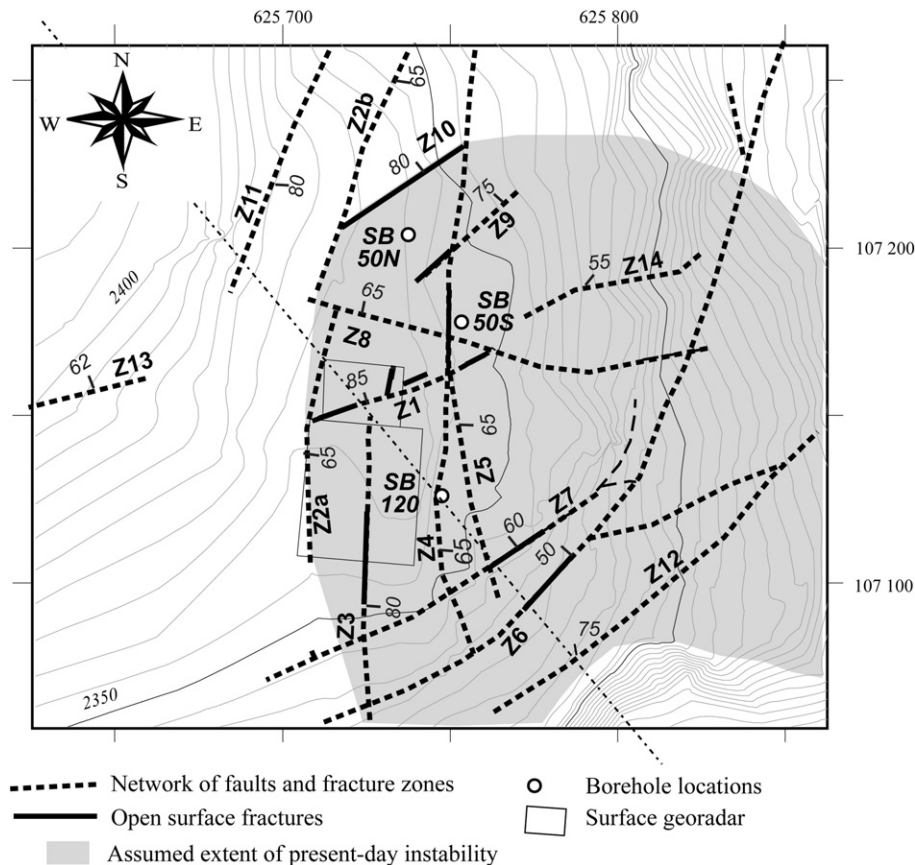

Fig. 10. Detailed map of faults and fracture zones within the study area. Dip direction and dip angles are marked along the traces. Foliation parallel faults (i.e. F-1) are not shown. Open surface fractures are drawn as solid lines. The thin NW–SE dashed line denotes the cross-section through the geological model (and SB 120) used to construct Fig. 17.
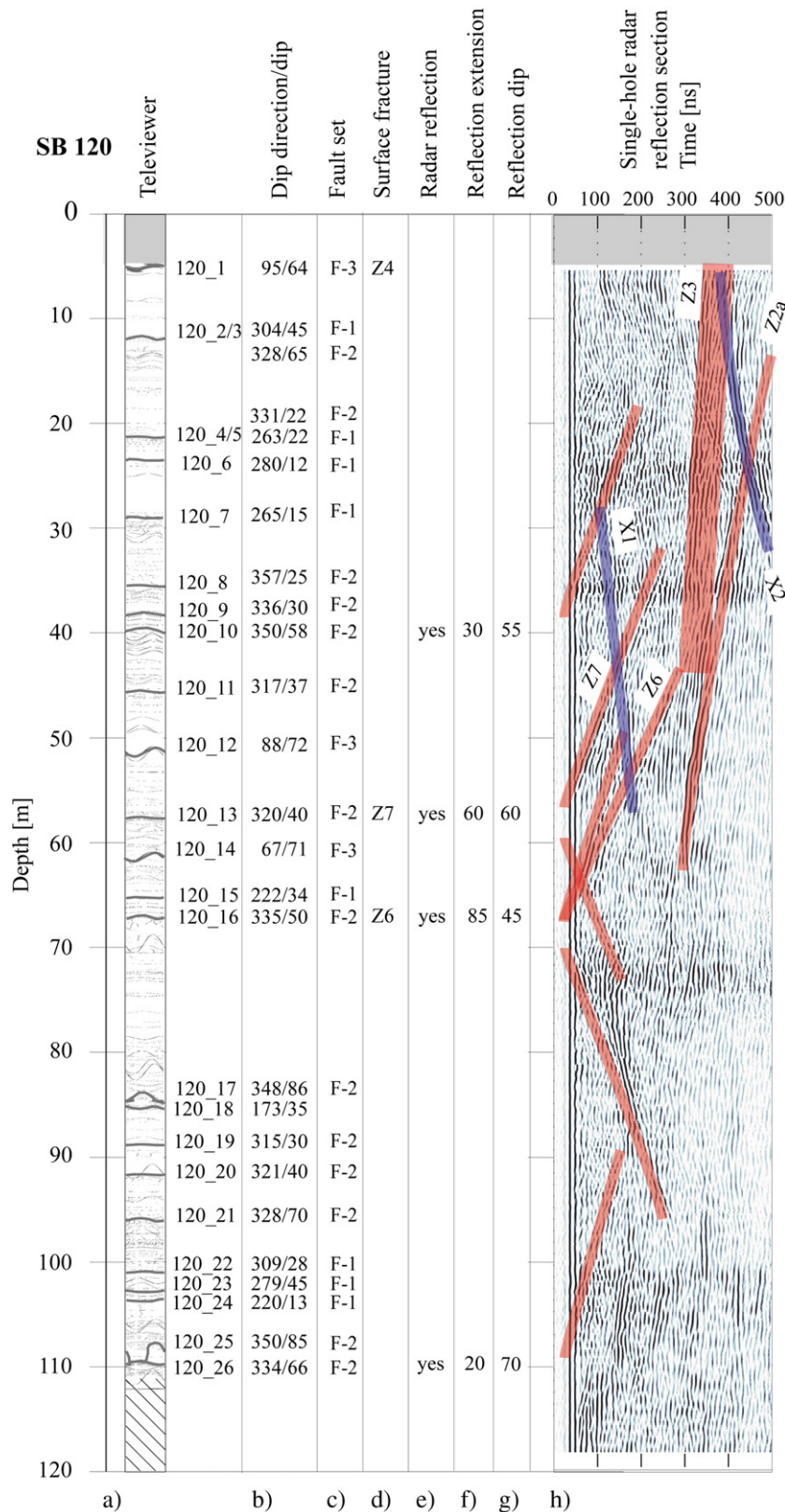
Fig. 11. Summary of borehole fracture data derived from the OTV log together with borehole georadar sections for SB 120. A total of 26 major fractures were identified on the OTV log. Of these, 4 belonging to the F-2 fault set could be associated with reflections in the georadar sections, such that their expression could be traced into the rock mass. a) Unwrapped OTV images of the fracture traces with the 26 major fractures highlighted and labeled. The hatched section below 111 m indicates the borehole was water-filled resulting in degraded image quality. b) Dip direction and dip of the faults and fracture zones. c) Fault set classification. d) Association with faults and fracture zones mapped at the surface, as suggested by geometrical constraints or borehole georadar data. e) Association with georadar reflections (see Spillmann et al., 2007). f) Minimum extent of the georadar reflections. g) Apparent dip of the georadar reflections. h) Single-hole radar section modified after Spillmann et al. (2007) with the most important reflections highlighted and labeled.

mean uniaxial compressive strengths of σ_{UCS}=97 MPa, which is comparable to those reported by Girod (1999). Lower values of σ_{UCS}=69 MPa were obtained for the fine grained *chloritic gneisses with small feldspar porphyroblasts*, which lie above the transition from unstable to stable ground.

Fracture orientations for the entire study area were found to be highly variable, which suggests that the mapped area incorporates several structural compartments (SC) with different preferred orientations. The degree of scatter in the data could be reasonably minimised by defining three structural compartments whose boundaries follow those of the lithological units (Fig. 6). Structural compartment SC I extends along the northern scarp of the 1991 rockslide boundary between 1900 to 2380 masl and includes the region of the current instability. Structural compartment SC II, immediately above SC I, comprises the chloritic gneisses, whereas SC III includes the top of the study area from 2440 to 2450 masl.

5.2. Fracture systems

Poles to all fractures (i.e. excluding faults and fracture zones) mapped within the three structural compartments are shown in the stereonets of Fig. 7. Foliation fractures are common and have the same orientation in each of the three structural compartments. A total of eight non-foliation fracture sets are recognised, with each individual structural compartment containing six to seven sets. Sets 1–5 are steep fractures that are dominant and appear in all structural compartments, with the exception of set 4 which is absent from SC I. Members of set 1 dip to the NE and are normal to both the foliation and the axis of the large recumbent fold of the Siviez Mischabel nappe. Sets 2–5 also include tectonic fractures related to the nappe structure

and stress release fractures. The wide scatter of these sets is most likely related to the presence of lithologic variability, large scale folding and faulting, and complex stress release features in the Matter valley which gradually changes its trend from N–S to E–W. None of the three moderately inclined fracture sets (6–8) are present in all three structural compartments. Set 6 was mapped mostly in SC II and III. In contrast, sets 7–8 primarily appear in SC I and thus are largely limited to the unstable part of the rock mass. Fractures belonging to set 7, which dip at 30–60° to the NW, are more frequent than those of set 8, which is in the opposite direction to the SE-directed movement of the unstable rock mass. As such, the set 7 fractures cannot play a significant role in the development of a basal sliding surface. The set 8 fractures dip shallowly to the south and are thus sub-parallel to the topographic surface of the unstable rock mass and its vector of movement. Hence, they are favourably oriented for accommodating sliding. However, their frequency and persistence is insufficient for them to serve as or to form an extensive basal or internal sliding surface (Willenberg, 2004). In terms of genesis, they are possibly unloading fractures, although their proximity to the foliation-parallel faults suggests a tectonic origin.

5.3. Faults and fracture zones

The network of steep to moderately inclined fault and fracture zones mapped in the study area is shown in Fig. 6. These were identified by combining results of surface mapping and analyses of aerial photographs with analyses of orthophotos of the region. The poles of faults and fracture zones are displayed in the stereonet of Fig. 8a. Those of major fractures/faults intersecting the boreholes (i.e. thickness of the trace on the OTV image >2 mm) are shown in Fig. 8b. These two
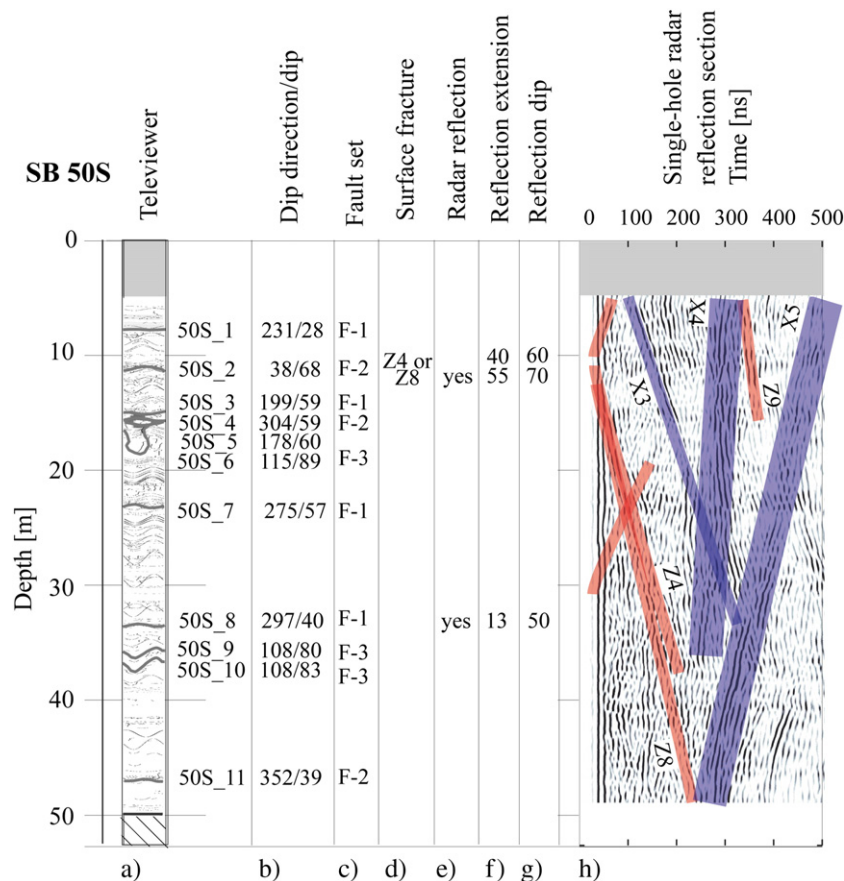

Fig. 12. Summary of borehole fracture data for borehole SB 50S. See Fig. 11 caption for details.
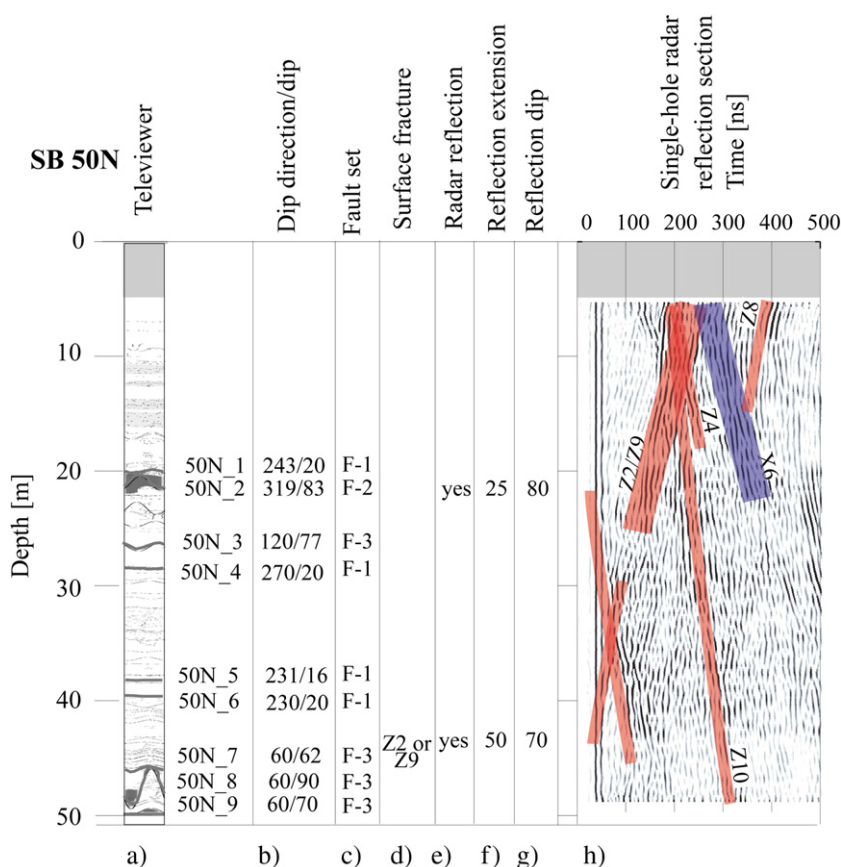
Fig. 13. Summary of borehole fracture data for borehole SB 50N. See Fig. 11 caption for details.

populations closely agree revealing the presence of three major fault sets. The first, denoted F-1, comprises mostly brittle–ductile shear zones that are oriented parallel to foliation. These are usually observed as pairs of parallel fractures bounding partly weakened phyllonitic bands with rotated blasts indicative of ductile shear (Fig. 9a). The bounding fractures commonly exhibit slickensides and are often accompanied by second-order en-échelon structures such as Riedel shears or extension joints. The F-1-faults are often associated with the set 8 auxiliary fractures (Fig. 9a). A schematic representation of a typical OTV image of an F-1

fault with a phyllonitic core is shown in Fig. 9d. The F-2 set includes brittle faults, brittle–ductile shear zones and fracture zones that exhibit fairly scattered orientations of dip between north and northwest. Most of the NW-dipping members, which are not accompanied by large damage zones, are usually mapped at the surface as large open discontinuities (Fig. 9b). The NW-dipping major fractures/faults inter-sected by the boreholes are either open or characterised by densely foliated, phyllonitic infillings as shown in Fig. 9e. Lastly, the F-3 set of faults and fracture zones strikes N–S, parallel to the valley. Morphological

Table 1
Comparison of estimates of the geometry of faults and fracture zones mapped on surface with estimates derived from borehole OTV, and borehole and surface georadar imaging

Fault	Fault set	Dip/dip direction on surface [°/°]	Dip/dip direction on OTV [°/°]	Borehole georadar reflections			Surface georadar reflection		Surface georadar diffraction pattern	
				Imaged	Dip [°]	Extent [m]	Imaged	Dip [°]	Imaged	Extent [m]
Z 1	F-2	350/85		No			No		(Yes)[a]	5
Z 2a	F-2	100/65		Yes	74	80	Yes[b]		No	
Z 2b	F-3	100/65		Yes	70	50	No		No	
Z 2c		Not mapped		No			Yes	40	Yes	30
Z 3	F-3	90/80		Yes	85	50			Yes	30
Z 4	F-3	100/65	95/64	Yes	60–70	60				
Z 5	F-3	90/65		No						
Z 6	F-2	330/50	335/50	Yes	45	85				
Z 7	F-2	325/60	320/40	Yes	60	60				
Z 8	F-2	05/65		Yes	75	10–55[c]				
Z 9	F-2	330/75		Yes	70	20				
Z 10	F-2	340/80		Yes	80	50				
Z 11	F-3	100/80		No						
Z 12	F-2	350/75								
Z 13	F-2	335/62								
Z 14		32/55		No						

[a] Only in the upper 5–7 m, not shown in Fig. 14a.
[b] Only on unmigrated data (see Spillmann et al., 2007).
[c] Determined at different locations along the fault/fracture zone.

depressions are commonly associated with these structures, but exposures in outcrops are scarce. Large fracture zones with or without a fault core are typical for this set (Fig. 9c).

It is evident from Fig. 6 that the density of faults and fracture zones is higher inside the estimated boundaries of the current slope instability than outside. A close-up of this area is shown in Fig. 10.
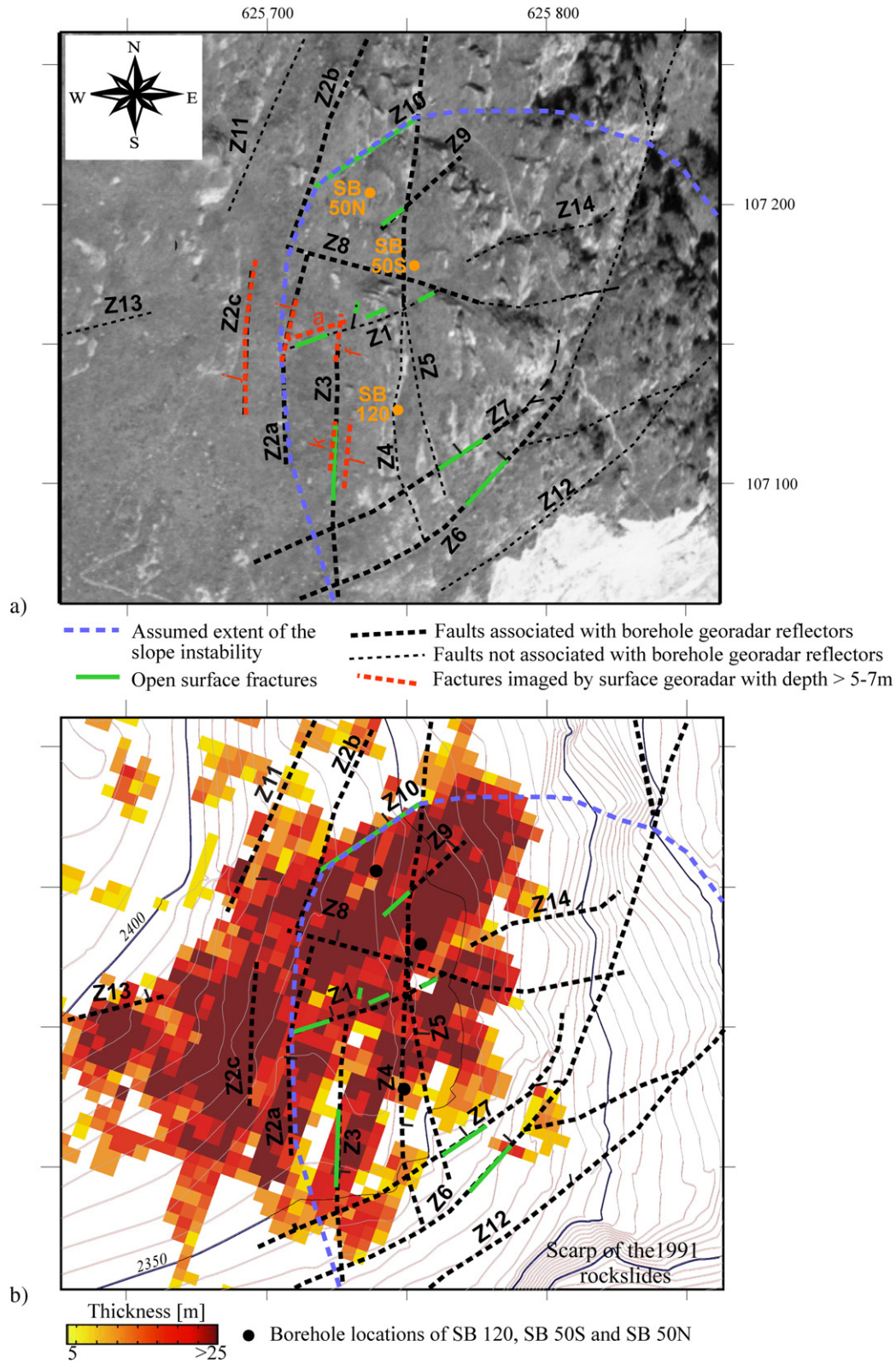

Fig. 14. a) Orthophoto of the study area with an overlay of fault and fracture zone traces inferred from mapping, lineament analysis and/or radar reflection surveys. The assumed extent of the instability is outlined with a blue dotted line. The green lines are segments of the faults and fracture zones that are open on surface. Faults and fracture zones that could be associated with borehole georadar reflectors are highlighted. The red dashed lines are high-angle planes indicated by high semblance values of the 3-D radar survey. The orthophoto is reproduced with permission of Swisstopo (BA068088). b) Thickness of ultralow velocity zones (<1500 m/s) determined from seismic refraction tomography (modified after Heincke et al., 2006b) with overlay of surface mapped faults and fracture zones. Thick ultralow velocity zones occur within the estimated boundaries of the unstable rock mass and beyond.
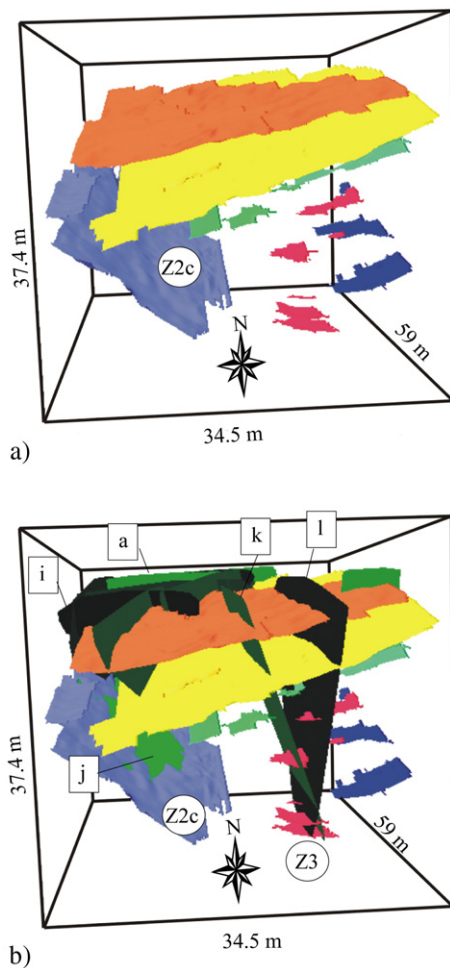
Fig. 15. Planar features imaged by the surface georadar surveys (modified after Heincke et al., 2006a). The 3-D representation provided includes the two survey areas as outlined in Fig. 10. a) Low-angle reflectors picked from the topographic-migrated data set. The orange reflector most likely corresponds to the bedrock surface. The persistent yellow feature that is parallel to foliation is probably an F-1 fault, and has been included as feature Z2c on the map of faults and fracture zones (Fig. 14). b) Same as a), but including high-angle planar features inferred from the semblance analysis.

The boreholes and surface traces of the individual faults and fracture zones are labeled Z1–Z14, in accord with the labelling used by Heincke et al. (2006a) and Spillmann et al. (2007). Open surface fractures are segments of mapped faults or fracture zones. It is important to note that no faults or fracture zones are positively identified (either at surface or in the boreholes) as dipping to the SE, sub-parallel to the surface measured slope displacements. Only one large feature that has this orientation is exposed on the rockslide scarp at 2150 masl. The precise nature of this feature is uncertain, due to its inaccessibility, although it has the appearance of a fracture. The absence of other faults or fracture zones with this orientation suggests that if it is a fracture, it may have formed during processes that led to the 1991 slope failures.

5.4. Imaging faults and fracture zones by surface and borehole georadar

Some of the mapped faults and fracture zones were imaged by the borehole and surface radar surveys, such that their orientations and locations could be confirmed and their minimum extent determined. Single-hole radar profiling and VRP reflection surveys imaged faults and fracture zones up to 30 m from the boreholes (Spillmann et al., 2007). A total of twenty-six major fractures were seen on the OTV images from SB 120. These are shown in Fig. 11 (televiewer) together

with their identification number, dip/dip direction and the fault set to which they belong. Of the twenty-six major fractures, four were imaged in the borehole reflection data. Two of these, which could be traced over a length of 60 m, were also correlated with surface fractures (120_13 with Z7; 120_16 with Z6). The shallow fracture 120_1 was also clearly associated with surface fracture Z4, but it was not resolved by the radar images. In SB 50S and SB 50N, two major fractures in each borehole could be identified in the georadar sections, two of which could be traced to a surface fault, albeit with some ambiguity (i.e. borehole fracture 50S_2 is connected to either Z4 or Z8, and SB 50N fracture 50N_7 to either Z2 or Z9; see Figs. 12h and 13h).

The georadar sections for all boreholes contained reflections that did not cut the boreholes and hence could not be uniquely oriented. There were 4 in each borehole data set. Attempts to identify surface faults or fracture zones that could explain these reflections yielded mixed results: surface faults with the sought characteristics could be identified for 2 reflections in SB 120, 3 in SB 50N and 1 in SB 50S. The six reflections for which no corresponding fault could be found may correspond to structures hidden beneath surficial vegetation or debris,
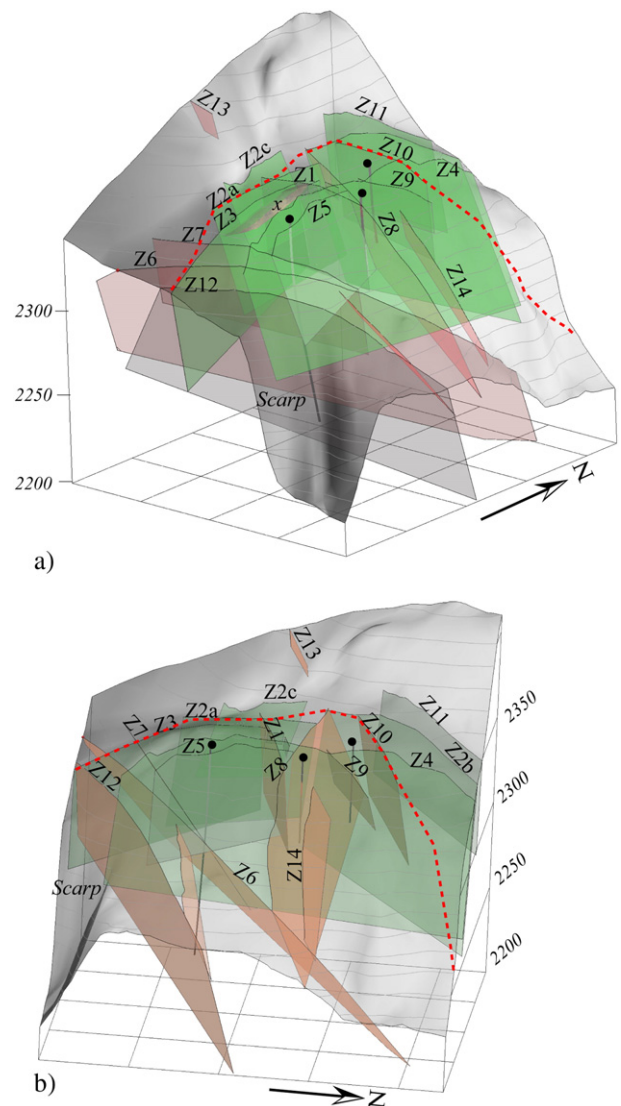

Fig. 16. Geological block model for the investigated area looking: (a) NW, and (b) W. Faults of the NW-dipping set F-2 are shown in red–brown, faults of the E to SE dipping set F-3 are shown in green–grey. The surface denoted 'x' corresponds to the prominent radar reflector shown in yellow in Fig. 15. The red dashed line denotes the assumed extent of the unstable rock mass. The tops of the boreholes are marked by black dots. The cell size of the bottom grid is 50×50 m.

or which do not extend to the surface. The analysis of the VRP data further constrained the extent of surface fault Z3. Additional details can be found in Spillmann et al. (2007).

A comparison of fault/fracture zone geometry obtained from surface mapping with data obtained from the borehole OTV images and the various radar reflection structures is given in Table 1 and illustrated in Fig. 14a. The continuity and scale of the faults and fracture zones on the surface suggest that they extend more than 80 m into the subsurface, a result supported by the single-hole radar surveys. Comparison of the dip angles of the radar reflections demonstrates that they generally agree with the mapped dips to within 10°. The dip estimates from the OTV are also in reasonable agreement, the primary discrepancy being for surface fault Z7, for which the OTV dip differs by 20° from that obtained from surface mapping and the borehole georadar data.

The two 3-D surface georadar surveys had a penetration depth of about 40 m (Heincke et al., 2005). Reflectors identified from the topographically migrated data set are shown in Fig. 15a in an image volume containing the two adjacent areas shown in Fig. 4. Since the majority are low-angle and parallel to foliation, they are likely F-1 faults. High-angle faults are absent because they do not give rise to reflections from the near-vertical incident waves. A prominent reflector that dips at 35–40° to the east, and thus cuts the foliation, can be seen on the left side of the image volume. This is undoubtedly a fault or fracture zone, but no mapped fault or lineament is present at its extrapolated intersection with the surface. Since it is closest to Z2a, it is designated Z2c. Its expected surface expression is included in the map of surface faults and fracture zones (Fig. 14).

High-angle faults and fracture zones with dips greater than 70° were imaged in the semblance-based migrated data set (Heincke et al., 2006a). This processing identified 13 steeply dipping planes, 6 of which extend further than 5 m into the rock mass. These 6 planes,

shown in Figs. 14a and 15b, largely coincide with faults and fracture zones mapped on the surface and reflectors identified in the single-hole radar data. A surprising result was that the prominent open surface fault Z1 (Fig. 14a) was seen to coincide with high semblance values in the uppermost 5 m, but not below.

5.5. P-wave velocity distribution

The P-wave velocities in the upper 30 m of the study area obtained from the surface seismic refraction survey range from 0.5 to 4.0 km/s (Heincke et al., 2006b). Extremely low velocities are found close to faults and fracture zones, particularly within the unstable rock mass. They extend to at least 30 m depth in some regions (see Fig. 14b). However, low velocities extending to depth are also found to the west of the estimated transition from unstable to stable rock. It is unlikely that such low velocities are related to lithology, because velocities greater than 3 km/s are found in the same units to the northwest. Rather, these extremely low velocities are evidence for very low quality, possibly unstable, rock that extends beyond the measured region of mobile rock. This zone may extend even further to the west (beyond the low velocities shown in Fig. 14b), but this could not be delineated with our deployment of seismic sources and receivers (Fig. 4).

6. Structural interpretation and conclusions

The combined geological and geophysical investigation has permitted a 3-D geological model of the complex internal structure of the unstable slope to be constructed (Fig. 16). The internal structure is dominated by steeply to moderately inclined faults and fracture zones that dip to the NW and E to SE (F-2 and F-3). The NW-dipping faults are prominent in the area near the boreholes, particularly at
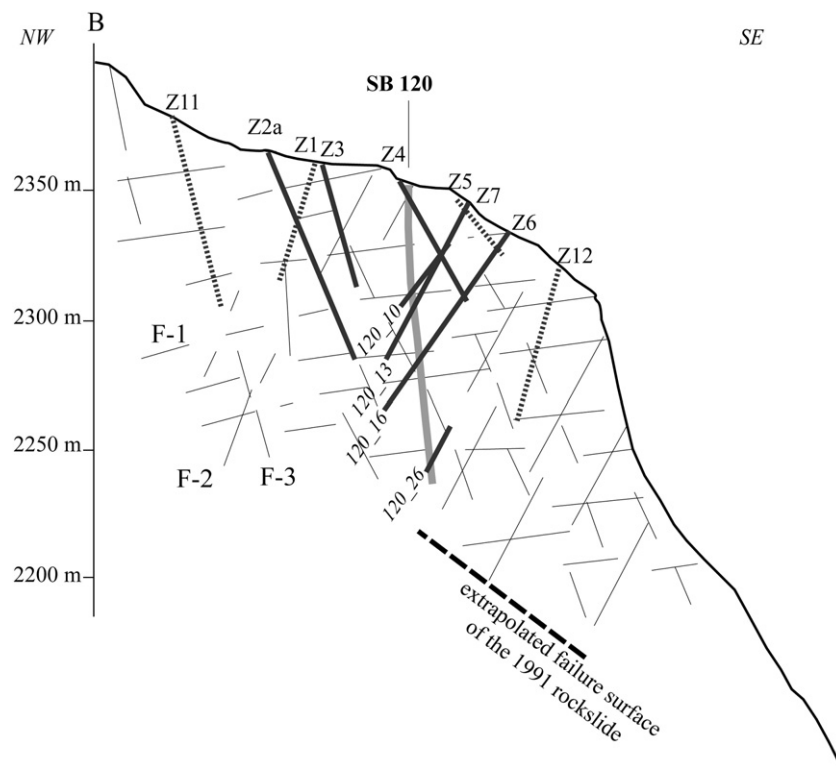

Fig. 17. NW–SE section through SB 120 showing the F-1 to F-3 fault/fracture sets. The location of the cross-section is shown in Fig. 10. Faults and fracture zones mapped by geological and geophysical methods are plotted as bold solid lines. Bold dashed lines indicate the location of surface faults and fracture zones that were not identified on the geophysical data or were situated outside the survey areas. Also shown is the approximate location of the extrapolated failure surface of the second 1991 rockslide, assuming a constant dip angle of 40° parallel to the debris covered failure surface and based on a rare SE-dipping feature on the scarp.

depth in SB 120 (Fig. 16b). Further to the NW, these faults are less persistent. The ESE-dipping faults dominate the rock mass near the western boundary of the unstable rock mass. This boundary likely follows the complex zone of faults and fracture zones Z2, Z3, Z2b, Z2c and Z11 (Fig. 16a).

The absence of clear lateral boundaries to the unstable rock mass may be linked to the multitude of faults and fracture zones that serve to dissect the slope into an assemblage of blocks. No clear through-going basal sliding surface, separating stable from unstable rock, dipping towards the valley has been identified. Several authors have proposed that the large inclined failure plane of the second 1991 rockslide (Fig. 2) extends under the study area (Sartori et al., 2003; Jaboyedoff et al., 2004). This plane dips at 140°/40° and is covered with debris above 1900 m, so its roughness and conformity to planarity are uncertain. A cross-section through the derived 3-D model (Fig. 17) shows the extrapolation of this plane under the study area. Given a dip of 40° it would not intersect SB 120; a dip greater than 41° would be required for it to intersect SB 120. Thus, its absence in SB 120 cannot be taken as evidence that it does not exist.

We emphasize that except for one large fracture-like feature observed on the rockslide scarp from a distance, there is no evidence for significant persistent faults or weakness planes that parallel the failure 'plane' of the second 1991 rockslide in surface outcrops, either in the borehole images or in the various geophysical data acquired at the study site. This suggests that the present rock slope instability may not be controlled by a pre-existing, highly persistent geological feature but instead may be developing through the progressive coalescence of small-scale discontinuities and the destruction of intact rock bridges. The time scale on which this process will occur is uncertain. Schindler et al. (1993) proposed that the hours-to-days duration of the 1991 rockslide events coincided with the development of the eventual failure plane. Although it is probable that the detailed demarcation and strength loss of the plane occurred during this period, the degree to which it had already been defined through progressive development and coalescence of discontinuities during the preceding phase of steady-state displacement is uncertain.

To address this question, it is of interest to establish the internal deformations that are occurring within the currently unstable rock mass, which is moving to the SE at a nearly constant rate (based on measurements carried out during the five year study period). These form the basis of the companion paper (Part II) in which we integrate the available surface and borehole deformation data in an attempt to place constraints on the kinematics of the unstable rock slope movements.

Acknowledgements

References

Bearth, P., 1964. Geologischer Atlas der Schweiz - Erläuterungen zum Blatt Randa. Geologischer Atlas der Schweiz 1:25000. Kümmerly & Frey, Bern. 27 pp.

Crosta, G.B., Agliardi, F., 2002. How to obtain alert velocity thresholds for large rockslides. Physics and Chemistry of the Earth 27, 1557–1565.

Eberhardt, E., Willenberg, H., Loew, S., Maurer, H.R., 2001. Active rockslides in Switzerland — understanding mechanisms and processes. In: Kühne, M., Einstein, H.H., Krauter, E., Klapperich, H., Pöttler, R. (Eds.), International Conference on Landslides — Causes, Impacts and Countermeasures. Verlag Glückauf, Davos, pp. 25–34.

Eberhardt, E., Stead, D., Coggan, J.S., 2004. Numerical analysis of initiation and progressive failure in natural rock slopes — the 1991 Randa rockslide. International Journal of Rock Mechanics and Mining Sciences 41 (1), 68–87.

Einstein, H.H., Veneziano, D., Baecher, G.B., O'Reilly, K.J., 1983. The effect of discontinuity persistence on rock slope stability. International Journal of Rock Mechanics and Mining Sciences 20 (1), 227–236.

Girod, F., 1999. Altération météorique de roche granitique en milieu alpin: le cas de l'othogneiss associé à l'éboulement de Randa (Mattertal, Valais, Suisse). Doctoral Thesis, Université de Lausanne, Lausanne, 207 pp.

Godio, A., Strobbia, C., De Bacco, G., 2006. Geophysical characterisation of a rockslide in an alpine region. Engineering Geology 83 (1–3), 273–286.

Grasmück, M., 1996. 3-D ground penetrating radar applied to fracture imaging in gneiss. Geophysics 61, 1050–1064.

Gruber, S., Hoelzle, M., 2001. Statistical modelling of mountain permafrost distribution: local calibration and incorporation of remotely sensed data. Permafrost and Periglacial Processes 12, 69–77.

Hack, R., 2000. Geophysics for slope stability. Surveys in geophysics 21, 423–448.

Heincke, B., Green, A.G., van der Kruk, J., Horstmeyer, H., 2005. Acquisition and processing strategies for 3-D georadar surveying a region characterized by rugged topography. Geophysics 70 (6), K53–K61.

Heincke, B., Green, A., van der Kruk, J., Willenberg, H., 2006a. Semblance-based topographic migration (SBTM): a method for identifying fracture zones in 3-D georadar data. Near Surface Geophysics 4, 79–88.

Heincke, B., et al., 2006b. Characterizing an unstable mountain slope using shallow 2- and 3-D seismic tomography. Geophysics 71 (6), B241–B256.

Ischi, H., Keusen, H.R. and Scheller, E., 1991. Randa, Kt. Wallis, Bergsturz Grossgufer vom April/Mai 1991 - Zusammenfassender Bericht über die Aktivitäten der Geotest AG. 91126, Geotest AG, Martigny.

Jaboyedoff, M., Ornstein, P., Rouiller, J.D., 2004. Design of a geodetic database and associated tools for monitoring rock-slope movements: the example of the top of Randa rockfall scar. Natural Hazards and Earth System Sciences 204 (4), 187–196.

Metternicht, G., Hurni, L., Gogu, R., 2005. Remote sensing of landslides: an analysis of the potential contribution to geo-spatial systems for hazard assessment in mountainous environments. Remote Sensing of Environment 98 (2–3), 284–303.

Müller, R., 1983. Die Struktur der Mischabelfalte (Penninische Alpen). Eclogae Geologicae Helvetiae 76 (2), 391–416.

Olsson, O., Falk, L., Forslund, O., Lundmark, L., Sandberg, E., 1992. Borehole radar applied to the characterization of hydraulically conductive fracture zones. Geophysical Prospecting 40, 109–142.

Ornstein, P., Jaboyedoff, M., Rouiller, J.D., 2005. RandaDB: un système de gestion de mesures appliqué a la surveillance des mouvements de versants, Géoline 2005. Lyon, p. 11.

Petley, D.N., Dunning, S.A., Rosser, N.J., 2005. The analysis of global landslide risk through the creation of a database of worldwide landslide fatalities. In: Hungr, O., Fell, R., Couture, R., Eberhardt, E. (Eds.), Landslide risk management. Taylor & Francis Group, Vancouver.

Ramsay, J.G., Huber, M.I., 1987. The Techniques of Modern Structural Geology — Folds and Fractures, 2. Academic Press Limited, London. 700 pp.

Sartori, M., Baillifard, F., Jaboyedoff, M., Rouiller, J.D., 2003. Kinematics of the 1991 Randa rockslides (Valais, Switzerland). Natural Hazards and Earth System Sciences 3, 423–433.

Schindler, C., Eisenlohr, T., 1992. Bergsturz Grossgufer bei Randa: Geologisch-geotechnische Expertise, Geologisches Institut ETH, Ingenieurgeologie, Zürich.

Schindler, C., Cuénod, Y., Eisenlohr, T., Joris, C.L., 1993. Die Ereignisse vom 18. April und 9. Mai 1991 bei Randa (VS) - ein atypischer Bergsturz in Raten. Eclogae Geologicae Helvetiae 86 (3), 643–665.

Schuster, R.L., 1996. Socioeconomic significance of landslides. In: Turner, A.K., Schuster, R.L. (Eds.), Landslides: Investigation and Mitigation. National Academy Press, Washington, pp. 12–35.

Spillmann, T., et al., 2007. Characterization of an unstable rock mass based on borehole logs and diverse borehole radar data. Journal of Applied Geophysics 61 (1), 16–38.

Tarchi, D., et al., 2003. Landslide monitoring by using ground-based SAR interferometry: an example of application to the Tessina landslide in Italy. Engineering Geology 68 (1–2), 15–30.

Tronicke, J., Knoll, M.D., 2005. Vertical radar profiling: influence of survey geometry on first-arrival traveltimes and amplitudes. Journal of Applied Geophysics 57 (3), 179–191.

Voight, B., 1989. Relation to describe rate-dependent material failure. Science 243 (4888), 200–203.

Wagner, A., 1991. Bergsturz Grossgufer Randa - Etude structurale et géomécanique, Centre de Recherches Scientifiques Fondamentales et Appliquées de Sion. Sion.

Willenberg, H., 2004. Geologic and kinematic model of a landslide in crystalline rock (Randa, Switzerland). PhD thesis Thesis, Swiss Federal Institute of Technology, Zürich, 184 pp.